

1 **Column-integrated Moist Static Energy Budget Analysis on**
2 **Various Time Scales during TOGA COARE**

3 KUNIAKI INOUE, * LARISSA BACK

University of Wisconsin-Madison, Madison, Wisconsin

* *Corresponding author address:* Kuniaki Inoue, Department of Atmospheric & Oceanic Sciences, University of Wisconsin-Madison, 1225 W. Dayton St., Madison, WI 53706.

E-mail: inoue2@wisc.edu

ABSTRACT

4
5 Moist static energy (MSE) budgets on different time scales are analyzed in the TOGA
6 COARE data, using Lanczos filters to separate variability with different frequencies. Four
7 different time scales (~ 2 day, ~ 5 day, ~ 10 day, and MJO time scales) are chosen based on the
8 power spectrum of the precipitation and previous TOGA COARE studies. The lag regression
9 slope technique is utilized to depict characteristic patterns of the variability associated with
10 the MSE budgets on the different time scales.

11 Our analysis illustrates that the MSE budgets behave in significantly different ways on the
12 different time scales. On shorter time scales, the vertical advection acts as a primary driver of
13 the recharge-discharge mechanism of column MSE. As the time scale gets longer, in contrast,
14 the relative contributions of the other budget terms become greater, and consequently, on the
15 MJO time scale all the budget terms have nearly the same amplitude. Especially, our results
16 indicate the horizontal advection plays an important role in the eastward propagation of the
17 MJO during TOGA COARE. On the MJO time scale, the export of MSE by the vertical
18 advection is in phase with the precipitation. On shorter time scales, the vertical velocity
19 profile transitions from bottom-heavy to top-heavy, while on longer time scales, the shape
20 becomes more constant and similar to a first baroclinic mode structure. This leads to a more
21 constant gross moist stability on longer time scales, which we estimate.

22 1. Background

23 In order to investigate the relationship between tropical convection and its associated
24 large-scale circulations, past work has examined column-integrated moist static energy (MSE)
25 budgets. These budgets tell us about the processes associated with the growth and decay of
26 column MSE. The column MSE is useful as a diagnostic quantity in the deep tropics primar-
27 ily for two reasons. First, it is approximately conserved in moist adiabatic processes, and it is
28 often beneficial to study any phenomenon from a perspective of conserved variables. Second,
29 the column MSE is tightly connected to tropical convective variability. Column water vapor
30 is known to be closely linked to precipitation anomalies in the tropics (e.g., Raymond 2000;
31 Bretherton et al. 2004; Neelin et al. 2009; Masunaga 2012), and temperature anomalies are
32 small due to the large Rossby radius (Charney 1963, 1969; Bretherton and Smolarkiewicz
33 1989; Sobel and Bretherton 2000). Together, these two constraints mean that the evolution
34 of column MSE is closely related to the evolution of precipitation anomalies. In this work,
35 we explore the charging and discharging mechanisms of column MSE that are associated
36 with precipitation anomalies for various frequencies of variability. To do this, we exam-
37 ine column MSE budgets using data from the Tropical Ocean Global Atmosphere Coupled
38 Ocean-Atmosphere Response Experiment (TOGA COARE; Webster and Lukas 1992) field
39 campaign.

40 The column-integrated MSE budget equation is, following Yanai et al. (1973),

$$\frac{\partial \langle h \rangle}{\partial t} = -\langle \vec{v} \cdot \nabla h \rangle - \langle \omega \frac{\partial h}{\partial p} \rangle + \langle Q_R \rangle + SF \quad (1)$$

41 where $h \equiv s + Lq$ represents MSE, s represents dry static energy (DSE), L represents the
42 latent heat of vaporization, q represents specific humidity, Q_R represents radiative heating
43 rate, SF represents surface fluxes of MSE, the other terms have conventional meteorology
44 meanings and we have neglected a residual due to ice processes. The angled brackets repre-
45 sent a vertical integral over mass in the troposphere. Because in the deep tropics variations
46 in the temperature field are much smaller than those of moisture, variations in h are pri-

47 marily due to fluctuations of atmospheric moisture. Thus investigating the column h budget
48 leads us to understand how moisture anomalies amplify and decay in the tropics.

49 Episodes of organized deep convection in the tropics are thought to generally begin with
50 bottom-heavy diabatic heating¹ that progressively deepens as the convection develops and
51 eventually becomes top-heavy and stratiform. This structure has been seen in convectively-
52 coupled equatorial waves (e.g., Takayabu et al. 1996; Straub and Kiladis 2003; Haertel and
53 Kiladis 2004; Haertel et al. 2008; Kiladis et al. 2009), the MJO (e.g., Lin et al. 2004; Kiladis
54 et al. 2005; Benedict and Randall 2007; Haertel et al. 2008), and even individual mesoscale
55 convective systems (e.g., Mapes et al. 2006). The vertical profile of convection also has a
56 strong impact on numerical simulations of the MJO (e.g., Lin et al. 2004; Fu and Wang 2009;
57 Kuang 2010; Lappen and Schumacher 2012, 2014), convectively-coupled waves (e.g., Cho and
58 Pendlebury 1997; Mapes 2000; Kuang 2008) and convective organization in general. These
59 phenomena are presently very challenging to simulate correctly, which makes numerical
60 weather prediction difficult (e.g., Lin et al. 2006; Kim et al. 2009; Benedict et al. 2013).

61 Interestingly, bottom-heavy profiles of vertical motion are associated with the import of
62 MSE by the vertical circulation (i.e., negative $\langle \omega \partial h / \partial p \rangle$). These tend to coincide with the
63 build-up of moisture in disturbances. Conversely, top-heavy profiles of vertical motion are
64 associated with the export of MSE by the vertical circulation and these tend to coincide
65 with the decay of moisture in disturbances. This suggests that, as pointed out by Peters and
66 Bretherton (2006), the vertical advection term could be playing a role in the charging and
67 discharging of column MSE associated with disturbances. This was also seen to some degree
68 in recent work on the MSE budget during the Dynamics of the Madden Julian Oscillation
69 (DYNAMO) field campaign (Sobel et al. 2014). In this work, we systematically examine
70 the relative contribution of this vertical advective term, as well as other terms to the build-

¹Since most of the diabatic heating is balanced by vertical DSE advection and profiles of the DSE are relatively constant in the tropics, structures of the diabatic heating are similar to those of the vertical velocity profiles.

71 up and decay of column MSE for various frequencies of variability observed during TOGA
72 COARE.

73 We also examine hypotheses about MJO dynamics that have been emerging from the
74 most recent MJO studies (e.g., Kim et al. 2014; Sobel et al. 2014). That is, 1) the radiative
75 heating and surface fluxes destabilize the MJO disturbance by amplifying and maintaining
76 MJO MSE anomalies while 2) the vertical advection stabilizes the disturbance by exporting
77 MSE, and 3) the horizontal advection plays a significant role in the eastward propagation
78 by building up moist conditions ahead, and providing dry conditions behind the active
79 convective phase. These points are investigated in the MJO events during TOGA COARE.

80 Neelin and Held (1987) introduced a normalized version of the vertical advective term,
81 known as the gross moist stability, which "provides a convenient way of summarizing our
82 ignorance of the details of the convection and large-scale transients." Other versions of this
83 quantity have been used in many studies (see a review paper by Raymond et al. 2009). In this
84 work, we examine the implications of the bottom-heavy to top-heavy evolution of vertical
85 motion profiles for the gross moist stability. We also briefly discuss an appropriate choice
86 of time filters for investigating relatively high frequency variability in the TOGA COARE
87 data set.

88 Section 2 describes our data and filtering, regression methodology. In section 3, we show
89 column-integrated MSE budgets for various time scales of variability, as well as vertical
90 motion profiles. Section 4 has a discussion of gross moist stability and calculations of this
91 quantity. In section 5, we discuss the relationship between a constant gross moist stability
92 and the vertical motion structure being well-described by a first baroclinic mode. In this
93 section, we estimate the gross moist stability in a different way from section 4 and also briefly
94 discuss sensitivity to our filter choice. In section 6, we describe our conclusions.

2. Data and Methodology

a. Data description

We investigated the data associated with the column-integrated moist static energy budget equation during the Tropical Ocean Global Atmosphere Coupled Ocean-Atmosphere Response Experiment (TOGA COARE; Webster and Lukas 1992). TOGA COARE is a package of various field experiments conducted in the western equatorial Pacific. The experiment provided detailed observations of the mean and transient states of the tropical variability in the western Pacific warm pool, enabling identification of the dominant dynamical and thermodynamic processes in large-scale tropical convective systems. We utilized the data during the Intensive Operative Period (IOP) starting from 1 November 1992 to 28 February 1993 with 6 hourly time resolution. Each variable was averaged over the spatial domain called the Intensive Flux Array (IFA; see Fig. 14 in Webster and Lukas 1992).

The data set we used was objectively constructed by Minghua Zhang, who used constrained variational analysis for producing each variable. That method guarantees the conservation of the column-integrated mass, water, and DSE. See Zhang and Lin (1997) for more detailed description about the constrained variational analysis.

b. Selection of time scales

For examining the column MSE budgets and associated terms for different frequencies of variability, we chose four time scales, ~ 2 day, ~ 5 day, ~ 10 day, and MJO (> 20 day) time scales. Those time scales are chosen based on a power spectrum of the precipitation during TOGA COARE and previous TOGA COARE studies. Figure 1a shows the power spectrum of the precipitation. Since the purpose of this study is not to investigate spectral signals which have been already examined by many previous studies, we will not look at statistical robustness of the signals in the power spectrum. We will use this power spectrum just for the purpose to determine which time scales should be separated to be investigated.

120 Figure 1a shows there are four peaks with different periodicities. The first one is the
121 diurnal cycle which is not of our interest in this study, thus was removed by filtering in
122 the analysis. The second peak can be found around 2 day period. This signal has been
123 investigated by Takayabu et al. (1996) and Haertel and Kiladis (2004) who have pointed out
124 that there exist westward propagating 2-day inertia gravity waves during TOGA COARE.
125 Thus we dealt with this time scale separately. The other signals are found around 4~5
126 day and 10~13 day periods, which could be Kelvin wave signals. Because those two are
127 obviously distinct and different from the 2-day wave signal, we also examined those time
128 scales separately. Because the signal of 10~13 day period in the power spectra is much
129 smaller than the other signals, we cannot negate the possibility that the signal here is just
130 a statistical noise. Nevertheless, we investigate this signal in order to keep consistency with
131 Mapes et al. (2006), who have also investigated this periodicity in the TOGA COARE data
132 set. Finally, the MJO time scale was extracted because many previous studies have shown
133 there are two MJO events during TOGA COARE (e.g., Velden and Young 1994; Lin and
134 Johnson 1996; Yanai et al. 2000; Kikuchi and Takayabu 2004) in late November to December
135 (around 30 to 65 COARE day) and in February (around 70 to 100 COARE day). Because the
136 second MJO signal was attenuated before reaching the IFA (see Fig.3 in Yanai et al. 2000),
137 most of the features in the following analyses on the MJO time scale reflect the structures
138 of the first MJO event.

139 *c. Filtering*

140 In order to extract different time scale features, a Lanczos filter was utilized. This
141 filter has been popularly used in meteorology and other areas because the responses of
142 frequencies to the filter has been well-studied (Duchon 1979) and it has desirable behaviors
143 with minimum Gibbs oscillations and relatively sharp cut-off slopes which prevent frequencies
144 of interest from being contaminated by undesirable leakage of frequencies and artificial false
145 responses produced by the Gibbs oscillations. We will briefly discuss sensitivities of the

146 results to the choice of filtering in section 5d, where we will compare the Lanczos filter with
147 a running mean filter, especially on short time scales.

148 There is a common trade-off between the number of weightings, or the number of data
149 points which have to be sacrificed, and desirable behaviors of the filter. We chose 151 as the
150 number of the weightings for all the analyses. This number was chosen in such a way that
151 the response function of the filter looks appropriate enough to separate the MJO signals from
152 the other shorter time scale signals (see Fig. 1b). Although we could have used a smaller
153 number for the analyses on the shorter time scales (~ 2 day and ~ 5 day scales) for reducing
154 sacrificed points, we used the same number for all the analyses. We tried different numbers
155 of weightings, and found those didn't make significant changes in the results. Figure 1c
156 shows time-series of the raw and filtered precipitation. We can see one strong MJO signal
157 from around 30 November 1992 to 3 January 1993 (from 30 to 65 COARE day) and one
158 weak signal from around 8 January to 7 February 1993 (from 70 to 100 COARE day).

159 *d. Regression analysis and correlation test*

160 Variability on the different time scales was plotted using a linear lag-regression analysis.
161 This method has been used by many studies (e.g., Kiladis and Weickmann 1992; Mapes et al.
162 2006). In this analysis, a predictand is regressed against a predictor (or a master index) to
163 determine regression slopes at different lag times. These computed regression slopes are
164 scaled with one standard deviation of the predictor so that the computed regression slopes
165 have the same unit as that of the predictand. We chose precipitation as the predictor,
166 and each variable in Eq. 1 as a predictand. We also computed the vertical structures of
167 the regression slopes of vertical pressure-velocity (ω), wind divergence, and specific
168 humidity on the different time scales as in Mapes et al. (2006). Those slopes were computed
169 at each lag time and each height. Both the predictor and predictands were filtered with a
170 Lanczos filter for statistical correlation tests. (For a regression analysis, predictands don't
171 need to be filtered.)

172 Statistical correlation tests were applied to test whether a given feature is statistically
 173 significant. Degrees of freedom (DOF) for the correlation tests were estimated at each lag
 174 and height following Bretherton et al. (1999). Although the values of the estimated DOF
 175 vary among different grids and variables, those variations are small enough that we neglect
 176 them. The DOF on ~ 2 day time scale is about 102 (this is an average value of the different
 177 values of the DOF) and the DOF on ~ 5 day time scale is about 22. On ~ 10 day time scale,
 178 the number of different realizations (convection) can be counted in Fig. 1c and it is about
 179 6, thus the DOF for the correlation test on this time scale is 4. For the MJO time scale,
 180 there are only two independent events. Since those numbers of the independent samples on
 181 10 day and the MJO time scales are too small to do statistical tests, statistical significance
 182 was tested only on ~ 2 day and ~ 5 day time scales.

183 **3. Results: Column MSE budgets and omega profiles**

184 *a. Column MSE budgets*

185 In the top panels of Fig. 2, plotted are lag auto-correlations of precipitation, lag cor-
 186 relations between precipitation and column-integrated MSE, and in the bottom panels lag
 187 regression slopes of each term in Eq. 1 regressed against the precipitation and scaled with
 188 one standard deviation of the precipitation on the different time scales. The standard de-
 189 viations of raw data, ~ 2 day, ~ 5 day, ~ 10 day, and MJO time scales, are respectively 229
 190 W m^{-2} , 112 W m^{-2} , 91 W m^{-2} , 121 W m^{-2} , and 123 W m^{-2} . Every variable is filtered with a
 191 Lanczos filter on the corresponding time scales. Confidence intervals of the 90% significant
 192 level of the regression slopes are also plotted on the left bottom corners on only ~ 2 day
 193 and ~ 5 day time scales; the time scales on which we can get enough DOF. The values of
 194 confidence intervals differ at different lags, thus average values among the lag time windows
 195 are plotted. The numbers on the right corners of each subplot are average values (among
 196 the lag time windows) of the numbers of the independent samples. Increased errors on ~ 5

197 day time scale compared to ~ 2 day time scale are primarily due to the reduced DOF.

198 We first acknowledge that due to the lack of DOF we are uncertain about whether or not
199 Figs. 2c and 2d represent statistically significant features of the MSE budgets on those time
200 scales. To examine statistical significance on those time scales, we need to investigate longer
201 time-series than the TOGA COARE data, which is left for future work. Nevertheless, we
202 can see that the patterns in Fig. 2d for the MJO events during TOGA COARE are similar
203 to those in Fig. 10 in Benedict et al. (2014) in which 10 year long ERA-interim and TRMM
204 with objectively analyzed surface flux data were investigated.

205 Column-integrated radiative heating $\langle Q_R \rangle$ is approximately in phase with the precipita-
206 tion (or the precipitation leads slightly) on all the time scales. Surface fluxes SF lag the
207 precipitation peaks on all the time scales except for ~ 10 day scale on which both radiative
208 heating and surface fluxes are nearly in phase with the precipitation. The lags of SF are
209 significant on ~ 5 day and MJO time scales (> 20 day).

210 The behaviors of column-integrated vertical MSE advection (or $-\langle \omega \partial h / \partial p \rangle$) differ among
211 the time scales. On ~ 2 day scale, positive advection (i.e., import of h) leads the precipita-
212 tion and the minimum value (i.e., maximum export of h) lags the precipitation peak. The
213 tendency of column-integrated h (or $\partial \langle h \rangle / \partial t$) agrees with the vertical advection term, which
214 implies that on this time scale most of the recharge-discharge cycle of h is explained by the
215 vertical advection while the other terms cancel out each other.

216 On the ~ 5 day scale, the pattern of vertical advection term is similar to that of ~ 2
217 day scale in which positive advection leads the precipitation and negative advection lags the
218 precipitation peak. Unlike the ~ 2 day scale, there is a lag between the vertical advection
219 and tendency term on this time scale which is due to negative contributions of the radiative
220 heating and surface fluxes in the early stage of the convection. This lag between the vertical
221 advection and tendency term becomes larger as the time scale gets longer.

222 On the ~ 10 day scale, the maximum vertical advection leads the tendency maximum by
223 around 3 days. Furthermore, the relative amplitude of vertical advection to the tendency

224 term becomes greater on this time scale, which is due to the other terms that work in the
225 opposite way to the vertical advection. That is, in the early stage of the convection the
226 vertical advection recharges the h while the other terms discharge the h and in the mature
227 stage the vertical advection exports the h while the other terms recharge it.

228 On the MJO time scale, akin to ~ 10 day scale, the positive vertical advection leads the
229 positive tendency term and amplitude of the vertical advection is greater than that of the
230 tendency term because the other terms play significant roles in the h budgets. It is also
231 worthwhile to note that as the time scale gets longer the vertical advective export of MSE
232 (i.e., positive $\langle \omega \partial h / \partial p \rangle$) becomes more in phase with precipitation peak (i.e., the lag relation
233 becomes closer to 180 degree out of phase). On ~ 2 day and ~ 5 day time-scales the vertical
234 advective h export lags the precipitation peak, while on ~ 10 day and the MJO time scale
235 it becomes more in phase with the precipitation peak. This in-phase h export pattern has
236 implications when we consider the gross moist stability (GMS), which will be discussed in
237 section 4b.

238 The horizontal advection (i.e., $-\langle \vec{v} \cdot \nabla h \rangle$) exhibits significantly different behaviors among
239 these different frequencies. On ~ 2 day scale, the positive horizontal advection leads the
240 precipitation and the minimum value reaches slightly after the precipitation peak. The hor-
241 izontal advection acts in almost opposite ways to the radiative heating and surface fluxes.
242 As a result, those terms cancel out each other. On ~ 5 day scale, the horizontal advection
243 is almost 90 degree out of phase with the precipitation. In contrast, on the ~ 10 day scale it
244 is almost in phase with the precipitation. Again, since Fig. 2c contains only 6 independent
245 samples we cannot conclude that this pattern is statistically robust. More detailed investiga-
246 tions should be done on this time scale in future work. On the MJO time scale, the horizontal
247 advection is 90 degree out of phase with the precipitation. Before the precipitation peak the
248 horizontal advection imports h while after the precipitation maximum it exports the h . As
249 the time scale gets longer, the amplitude of the variations of the horizontal advection be-
250 come greater, which might indicate that the relative contribution of the horizontal advection

251 to the recharge and discharge of the MSE becomes more important as the time scale gets
252 longer.

253 The relative amplitudes of each term indicate which terms are the most important for
254 these frequencies. For all the frequencies except for the MJO, the vertical advection domi-
255 nates the other terms which implies that the vertical advection is the most important h sink
256 and source. At longer time scales of variability (lower frequencies), however, the amplitude
257 of the vertical advection term relative to the source/sink terms becomes less. On the MJO
258 scale, the horizontal and vertical advection, radiative heating, and surface fluxes all have
259 relatively similar amplitudes. That indicates that all the terms in the MSE budgets play
260 important roles in the MJO dynamics.

261 Furthermore, the results shown in Fig. 2d on the MJO time scale reinforce the view of
262 the MJO dynamics which has been emerging from recent studies (e.g., Kim et al. 2014; Sobel
263 et al. 2014). That is, 1) the radiative heating and surface fluxes amplify and maintain the
264 MJO MSE anomalies while 2) the MJO disturbance is stabilized by the vertical advection
265 which exports MSE and cancels the effect of the radiative heating and surface fluxes, and
266 therefore 3) the eastward propagation of the MJO is primarily driven by the horizontal
267 advection which provides moistening ahead (in the negative lags, or to the east of), drying
268 behind (in the positive lags, or to the west of) the active convective phase. Although there
269 are differences between the different MJO events as pointed out by Sobel et al. (2014), our
270 results, in general, show significant consistencies with the results given by Kim et al. (2014)
271 and, to some degree, with the results in Sobel et al. (2014).

272 *b. Omega profiles*

273 Figure 3 shows vertical structures of vertical pressure velocity (omega) and wind diver-
274 gence on the different time scales. The areas surrounded by the green curves passed statistical
275 correlation tests with 99% (on ~ 2 day time scale) and 80% (on ~ 5 day time scale) significant
276 levels. The lower significant level used on ~ 5 day time scale is because of smaller DOF on

277 this time scale compared to ~ 2 day time scale. The statistical tests were not applied for
278 ~ 10 day and the MJO time scales due to the lack of DOF. As Mapes et al. (2006) showed,
279 we can observe tilting structures of the omega profiles in which the profile evolves from a
280 bottom-heavy shape into a top-heavy shape (indicated by the black dash lines), and these
281 tilting structures are statistically significant. The figures of the wind divergence illustrate the
282 same information as the omega figures. Height of the lower tropospheric convergence (blue
283 shaded contours) rises as the convection develops, making the tilting divergence profiles.

284 However, one can notice that the tilt of the omega profile becomes steeper as the time
285 scale gets longer. Especially, on the MJO time scale, the contour line of the omega is
286 almost perpendicular to the isobaric surface at -10 lag day. There is a shallow convective
287 phase on this scale, too (see from -22 to -12 lag days), but this shallow convection is
288 more abruptly changed into deep convection compared to those on the shorter time scales in
289 which the transitions of the convection from a bottom-heavy to a top-heavy shape happen
290 more gradually. The divergence figures depict the differences among the time scales clearly.
291 In the upper troposphere, the structures are qualitatively similar among the different time
292 scales. In the inactive stage of the convection, strong convergence associated with upper
293 tropospheric descending motion happens at the top of the troposphere. In the mature stage
294 of the convection, in contrast, strong divergence due to deep convection happens.

295 In the lower half of the troposphere, differences among the time scales are prominent.
296 On all the time scales except for the MJO time scale, in the inactive convective stage,
297 the strongest divergence happens around 600 hPa. On the MJO time scale, in contrast,
298 the divergence at this level is much weaker than that on the shorter time scales, and the
299 strongest divergence happens around 900 hPa. This lower tropospheric divergence maintains
300 its strength until -15 lag day. As this lower tropospheric divergence disappears, the convec-
301 tion abruptly changes into deep convection. Therefore, on the MJO time scale, the omega
302 profiles behave like a single deep convection mode which is often called a first baroclinic
303 mode. This omega behavior has implications regarding the gross moist stability (GMS) of

304 the convective system.

305 Before going to the next section, it should be emphasized again that the results shown
306 in Figs. 3g and h reflect only two MJO events, one of which is a weak event, and thus it is
307 almost a case study. Therefore, it is difficult to draw a general conclusion about the MJO
308 structures from our analysis particularly because the details of the MJO structures differ
309 significantly from event to event. However, we can at least claim that a strong tilt of the
310 omega profile (or latent heating profile) is not necessary for the existence of the MJO even
311 though the tilt might play a role in the MJO dynamics.

312 Furthermore, it should also be noted that our lag-regression methodology extracted the
313 actual structures of the MJO event during TOGA COARE in an appropriate way. Figure
314 4 shows the time-height plot of the anomalous omega of the first MJO event during TOGA
315 COARE, which occurs between ~ 30 COARE day and ~ 65 COARE day. In this plot, we
316 simply utilized a 15-day running mean filter. Although the contour is noisy due to the noise
317 introduced by the running mean filter, the overall structure is similar to that in Fig. 3g.
318 This figure indicates that our methodology captures the MJO structures well, and negates
319 the possibility that the result shown in Fig. 3g is due to a false signal introduced by the
320 statistical method.

321 **4. More results: Gross moist stability**

322 *a. GMS with different frequencies*

323 Now the gross moist stability (GMS) on the different time scales will be computed.
324 Before doing actual computations, the concept of the GMS needs to be clarified. The GMS,
325 which is a concept originated by Neelin and Held (1987), represents the efficiency of MSE
326 export by convection and associated large-scale circulations. Raymond et al. (2009) defines
327 a relevant quantity called normalized GMS (NGMS), which is a ratio of column MSE (or
328 moist entropy) advection to intensity of the convection. Although different authors have used

329 slightly different definitions of the NGMS (e.g., Fuchs and Raymond 2007; Raymond and
 330 Fuchs 2009; Raymond et al. 2009; Sugiyama 2009; Andersen and Kuang 2011), the physical
 331 implications behind those definitions are consistent in such a way that the NGMS represents
 332 efficiency of export of some intensive quantity conserved in moist adiabatic processes per unit
 333 intensity of the convection (Raymond et al. 2009). We employ one version of the NGMS
 334 defined as

$$\Gamma = \frac{\langle \vec{v} \cdot \nabla h \rangle + \langle \omega \frac{\partial h}{\partial p} \rangle}{\langle \vec{v} \cdot \nabla s \rangle + \langle \omega \frac{\partial s}{\partial p} \rangle} \quad (2)$$

335 where h and s represent MSE and DSE, respectively. Since in the tropics, horizontal tem-
 336 perature gradients are negligible (weak temperature gradient; Sobel and Bretherton 2000),
 337 neglecting the horizontal DSE advection in the denominator yields

$$\Gamma = \frac{\langle \vec{v} \cdot \nabla h \rangle + \langle \omega \frac{\partial h}{\partial p} \rangle}{\langle \omega \frac{\partial s}{\partial p} \rangle}. \quad (3)$$

338 Equation 3 can be separated into horizontal and vertical components as

$$\Gamma = \Gamma_h + \Gamma_v \quad (4)$$

339 where

$$\Gamma_h = \frac{\langle \vec{v} \cdot \nabla h \rangle}{\langle \omega \frac{\partial s}{\partial p} \rangle}$$

$$\Gamma_v = \frac{\langle \omega \frac{\partial h}{\partial p} \rangle}{\langle \omega \frac{\partial s}{\partial p} \rangle}.$$

341 In some NGMS studies, the vertical component of the NGMS Γ_v is simply called NGMS
 342 (or GMS) (e.g., Sugiyama 2009; Kuang 2010; Andersen and Kuang 2011; Sobel and Maloney
 343 2012) while in the others, the horizontal component Γ_h is explicitly defined (e.g., Raymond
 344 and Fuchs 2009; Raymond et al. 2009; Benedict et al. 2014; Hannah and Maloney 2014;
 345 Sobel et al. 2014). Γ_v has been used in various ways such as a diagnostic quantity in general
 346 circulation models (e.g., Frierson 2007; Hannah and Maloney 2011, 2014; Benedict et al.
 347 2014), in observational data (e.g., Yu et al. 1998; Sobel et al. 2014)², as an output quantity

²In Yu et al. (1998), the computed quantity was GMS, and not normalized one.

348 of a MJO toy-model (e.g., Raymond and Fuchs 2009), and as an input parameter of a MJO
349 toy-model (e.g., Sugiyama 2009; Sobel and Maloney 2012, 2013). As Hannah and Maloney
350 (2011) and Masunaga and L’Ecuyer (2014) pointed out, values of Γ_v generally fluctuate
351 in convective life-cycles primarily due to variations of vertical velocity profiles (as seen in
352 Fig. 3). Nevertheless, when used as an input parameter of a toy-model, Γ_v is assumed to
353 be a constant in the convective life-cycle (e.g., Sugiyama 2009; Sobel and Maloney 2012).
354 Furthermore, time-dependent fluctuations of the NGMS are also neglected when the NGMS
355 is computed based on scatter plots between the numerator and denominator of the NGMS,
356 which is one of the most general methods to compute the NGMS.

357 When considering the NGMS on different time scales in data, we have to be careful
358 about its interpretation. First of all, we can define a mean NGMS, in which we average
359 the numerator and the denominator of Γ before taking the ratio. This is in keeping with
360 the spirit of the definition. We can also define an anomalous NGMS, in which perturbations
361 from the means of numerator and denominator are taken and the ratio of these perturbations
362 is computed. Similarly, we can define a total NGMS³. It can be easily shown that the total
363 NGMS is a constant if and only if the mean NGMS is equal to the anomalous NGMS. In
364 many of previous studies, the total NGMS has been assumed to be constant. In such cases,
365 one doesn’t have to worry about the differences between the mean and anomalous NGMS.
366 But when considering the total NGMS as a time-dependent variable, one should clarify which
367 kinds of NGMS are being used, mean, anomalous, or total NGMS.

368 Furthermore, we can generalize the idea of the decomposition of the NGMS from an
369 aspect of Fourier transformation. By taking Fourier decomposition, Eq. 1 can be separated
370 into

$$\frac{\partial \langle h \rangle_i}{\partial t} = -\langle \vec{v} \cdot \nabla h \rangle_i - \langle \omega \frac{\partial h}{\partial p} \rangle_i + \langle Q_R \rangle_i + SF_i \quad (5)$$

³The phrase ”total NGMS” is often used to refer to the combination of Γ_h and Γ_v . In this study, we use the phrase ”total NGMS” to refer to the combination of anomaly and mean state. Γ_h plus Γ_v is simply called NGMS or Γ in this paper.

371 where subscripts represent a specific range of frequencies. For instance, $i = 0$ can be defined
 372 as the mean state, and $i = ISO$ can be defined so that Eq. 5 represents intra-seasonal
 373 oscillations as in Maloney (2009). Therefore, we can define the NGMS on different time
 374 scales as

$$\Gamma_i = \frac{\langle \vec{v} \cdot \nabla h \rangle_i + \langle \omega \frac{\partial h}{\partial p} \rangle_i}{\langle \omega \frac{\partial s}{\partial p} \rangle_i}. \quad (6)$$

375 The horizontal and vertical components on different time scales can be defined similarly to
 376 Eq. 4.

377 Interpretations of the sign of the NGMS also require some attentions. When dealing
 378 with band-pass filtered variability, the denominator of Eq. 6 represents anomalous quanti-
 379 ties which can be both positive and negative. With a positive denominator (this is a usual
 380 case when convection is active), positive/negative NGMS corresponds to export/import of
 381 the MSE. But, when the denominator is negative (or when convection is inactive), the inter-
 382 pretation must be reversed; that is, a positive/negative value corresponds to import/export
 383 of the MSE.

384 *b. NGMS during TOGA COARE*

385 We estimated the time-dependent NGMS on the four different time scales using Eq. 6.
 386 Figure 5 shows the lag regression slopes of horizontal (blue), vertical (red), and combined
 387 (green) column-integrated MSE advection as a function of lag regression slopes of column-
 388 integrated vertical DSE advection on the different time scales. The elliptic shapes represent
 389 life-cycles of convection in which each life-cycle starts from a filled circle, going around
 390 counterclockwise, and terminates at a filled square. Γ_h , Γ_v , and Γ at different convective
 391 phases can be estimated by computing the slopes of the lines which are drawn from the
 392 origin to the periphery of the elliptic shapes. For instance, on ~ 2 day scale, Γ_v starts
 393 with a positive value (~ 0.2) which becomes larger and goes infinity (this corresponds to the
 394 singularity of the NGMS). After passing through the singular point, it becomes negative

395 which grows into a positive value and reaches about 0.2 again at the peak of the convection.
396 After the convective peak, Γ_v increases and becomes infinity again at the singular point,
397 followed by negative values.

398 One conclusion we can draw from Fig. 5 is that the NGMS and all the components are
399 not constant values on all the time scales, but they vary along the convective life-cycle. But
400 we can find that as the time scale gets longer the vertical NGMS Γ_v converges to a constant
401 value around 0.2, which is the slope of the major axis of the elliptic shape. On the MJO
402 time scale, the elliptic shape of the vertical MSE advection becomes very close to a linear
403 shape (i.e., constant Γ_v) with the minor axis collapsed. This more-constant Γ_v is related to
404 the fact that the column-integrated vertical MSE advection becomes closer to 180 degree
405 out of phase (negatively in phase) with the precipitation as the time scale gets longer. This
406 indicates that on longer time scales, the column-integrated vertical MSE advection is more
407 linearly correlated to the precipitation. This result might support one of the popular usages
408 of Γ_v in a MJO toy-model in which Γ_v is assumed be a time-independent quantity (e.g.,
409 Sugiyama 2009; Sobel and Maloney 2012).

410 Compared with the vertical advection, the horizontal advection doesn't have a consistent
411 pattern among the different time scales. On ~ 2 day scale, the major axis of the ellipse
412 of the horizontal advection has a positive slope while on ~ 5 day scale the slope is almost
413 zero. In contrast, on ~ 10 day scales, it has a negative slope. On the MJO scale, its slope
414 is slightly positive, but the values of Γ_h vary significantly during the convective life-cycle.
415 As a result, the NGMS Γ (combination of Γ_h and Γ_v) also varies significantly during the
416 convective life-cycles on all the time scales. It should also be noted that the elliptic patterns
417 of Γ are more similar to those of Γ_v than those of Γ_h on all the time scales except for the
418 MJO time scale.

5. Discussion

a. Omega profiles and Γ_v

Most of the variations in $\langle \omega \partial h / \partial p \rangle$ are explained by the variations of the omega profiles (94% of the total variance in the TOGA COARE data), and the variations of the MSE profiles play a small role. We can use the assumption that omega profiles can be approximated by two dominant modal structures to reason about the importance of each mode for the column MSE budget. We assume

$$\omega(t, p) \approx o_1(t)\Omega_1(p) + o_2(t)\Omega_2(p) \quad (7)$$

where Ω_1 and Ω_2 are often called first and second baroclinic modes, respectively, and o_1 and o_2 represent the time-dependent amplitudes of those modes. These could be any two modes which do a good job of describing the variability in vertical motion profiles, like those that come from a principle component analysis of vertical motion profiles. In the TOGA COARE data, the first mode of a principle component analysis (PCA) explains 71% of the variance, and the second mode explains 21% of the total variances of the omega profiles.

If we neglect the variations of the MSE profiles, we can represent Γ_v as

$$\Gamma_v \approx \frac{o_1 \langle \Omega_1 \frac{\partial \bar{h}}{\partial p} \rangle + o_2 \langle \Omega_2 \frac{\partial \bar{h}}{\partial p} \rangle}{o_1 \langle \Omega_1 \frac{\partial \bar{s}}{\partial p} \rangle + o_2 \langle \Omega_2 \frac{\partial \bar{s}}{\partial p} \rangle} \quad (8)$$

where the bars represent the time averages.

In general, the MSE and DSE profiles, Ω_1 and Ω_2 , if chosen via PCA, have the structures as shown in the schematic figure, Fig. 6. In the first baroclinic system, convergence happens in the lower troposphere where the DSE is poor and divergence happens in the upper troposphere where the DSE is rich. Hence, in this system, strong net export of DSE happens (i.e., $\langle \Omega_1 \partial \bar{s} / \partial p \rangle$ is positive and large). In contrast, in the second baroclinic system, convergence happens both in the lower and upper troposphere where the DSE is poor and rich, respectively, and divergence happens in the middle troposphere where the DSE is moderate. As a result, the upper tropospheric net import of DSE is canceled out by the lower tropospheric

442 net export of DSE, causing small value of $\langle \Omega_2 \partial \bar{s} / \partial p \rangle$. Consequently, the value of $\langle \Omega_1 \partial \bar{s} / \partial p \rangle$
 443 is much larger than $\langle \Omega_2 \partial \bar{s} / \partial p \rangle$. Neglecting $\langle \Omega_2 \partial \bar{s} / \partial p \rangle$ in Eq. 8 yields

$$\Gamma_v \approx \frac{\langle \Omega_1 \frac{\partial \bar{h}}{\partial p} \rangle}{\langle \Omega_1 \frac{\partial \bar{s}}{\partial p} \rangle} + \frac{o_2 \langle \Omega_2 \frac{\partial \bar{h}}{\partial p} \rangle}{o_1 \langle \Omega_1 \frac{\partial \bar{s}}{\partial p} \rangle}. \quad (9)$$

444 This equation shows that for this set of assumptions, time-dependent fluctuations Γ_v are due
 445 to the second term in the rhs of Eq. 9, which is the ratio of the amplitude of the second
 446 mode to that of the first mode times the ratio of the gross moist stability due to the second
 447 mode to the gross dry stability (the denominator of Γ_v ; Yu et al. 1998) due to the first mode.
 448 In general, $\langle \Omega_2 \partial \bar{h} / \partial p \rangle$ is negative and large while $\langle \Omega_1 \partial \bar{h} / \partial p \rangle$ is positive and small (based on
 449 Fig. 6 and similar arguments to those for the gross dry stability $\langle \Omega_1 \partial \bar{s} / \partial p \rangle$ and $\langle \Omega_2 \partial \bar{s} / \partial p \rangle$).
 450 Thus, for this set of assumptions, the second term in the rhs of Eq. 9 is responsible for
 451 negative Γ_v in the early stage of the convection, as pointed out by Hannah and Maloney
 452 (2011) and Masunaga and L'Ecuyer (2014). This term is also responsible for the nonlinearity
 453 of the vertical MSE advection with respect to the convection, making the elliptic trajectories
 454 in Fig. 5. If this time-dependent term disappears, Γ_v given by Eq. 9 is the homomorphism
 455 of the GMS given by Neelin and Held (1987).

456 In Fig. 3, we showed that as the time scale gets longer, the tilting structure of the
 457 omega profile becomes less prominent. This disappearance of the tilt is likely due to smaller
 458 contributions of the second baroclinic mode on longer time scales compared to those on
 459 shorter time scales. This indicates that the second term in the rhs of Eq. 9 becomes smaller
 460 as the time scale gets longer, making Γ_v a more time-independent quantity. On shorter
 461 time scales where the second baroclinic mode is prominent, in contrast, the time-dependent
 462 term in Eq. 9 is robust, hence Γ_v on those time scales varies significantly in the convective
 463 life-cycles.

464 Some studies have argued for an important role of shallow convection in the convective
 465 variability including the MJO in which shallow convection enhances moisture import via
 466 enhanced surface convergence, and thus amplifies the convective system (e.g., Wu 2003;
 467 Kikuchi and Takayabu 2004). In our results, although it was less significant than the deep

468 convective profile, a shallow convective phase can be observed even on the MJO time scale.
469 That shallow convection could play a role in the MJO dynamics.

470 Interestingly, the elliptic trajectories shown in Fig. 5 have been already pointed out
471 by Masunaga and L'Ecuyer (2014), who investigated the MSE budgets and computed the
472 time-evolution of the NGMS on short time scales using the satellite data sets. There are
473 a few notable differences between our analysis and their study. First, they used a different
474 NGMS definition, which is a ratio of MSE advection to moisture advection instead of DSE
475 advection. Therefore, their NGMS plot is a mirror image of our NGMS plot with respect to
476 the x-axis (see Fig. 13 in Masunaga and L'Ecuyer (2014)). Second, they computed the total
477 NGMS including the background state instead of the anomalous NGMS which we computed.
478 Thus the center of the elliptic shape is shifted to the right and downward. The composite
479 methodology is also different from our study. Nevertheless, their study has drawn a similar
480 conclusion about the NGMS variability to ours. That is, the first/second baroclinic modes
481 explain the larger (along the major axis)/smaller (along the minor axis) variability of the
482 elliptic trajectory.

483 *b. How to compute NGMS*

484 The values of estimated NGMS depend on the method of the computation. In section
485 4, we showed the NGMS as a time-dependent variable. But in some recent NGMS studies,
486 NGMS is computed based on a scatter plot of MSE advection as a function of DSE advection
487 (e.g., Raymond and Fuchs 2009). In such a case, time-dependent fluctuations are not taken
488 into account.

489 If we estimate the NGMS following that method, then the values of the NGMS, the
490 horizontal and vertical components correspond to the slopes of the major axes of the elliptic
491 trajectories in Fig. 5. The values of those slopes ($\bar{\Gamma}$, $\bar{\Gamma}_h$, and $\bar{\Gamma}_v$) are summarized in Table 1.
492 As discussed above, $\bar{\Gamma}_h$ varies significantly among the time scales. Consequently, $\bar{\Gamma}$ which is
493 the combination of $\bar{\Gamma}_h$ and $\bar{\Gamma}_v$ also varies among the different time scales. Although smaller

494 than the variations of $\bar{\Gamma}$ and $\bar{\Gamma}_h$, there are variations of $\bar{\Gamma}_v$ among the time scales, too. These
495 might be due to the variations of the shapes of Ω_1 among the different time scales, which
496 could be caused by errors due to the small number of the independent samples.

497 *c. Tilt in other work*

498 Mapes et al. (2006, hereafter M06) proposed the "Stretched Building Block" hypothesis
499 that "individual cloud systems in different phases of a large-scale wave have different dura-
500 tions of shallow convective, deep convective, and stratiform anvil stages in their life cycles."
501 This hypothesis was proposed to explain the apparent multi-scale similarities of the vertical
502 structures between the mesoscale convective systems, convectively coupled equatorial waves,
503 and the MJO. The systematic steepening of the leading edge slopes in the omega profiles
504 shown in Fig. 3 suggest that omega may not have as much multi-scale similarity as M06
505 suggested, especially on the MJO time scale.

506 The wind divergence field on the MJO time scale in our result (Fig. 3h) resembles that
507 in M06 (the second panel of Fig. 8 therein), both of which contain a small amount of tilt.
508 However, that tilt is, as shown in section 3b, too small to claim the multi-scale similarity of
509 the omega profiles, especially on the MJO time scale. In contrast, a significant multi-scale
510 similarity is observed in the specific humidity field. Figure 7 shows the time-height structures
511 of specific humidity on the different time scales and there is significant tilt on all time scales,
512 unlike in vertical motion. Our figure is consistent with Fig. 7 in M06, which is given as
513 evidence for the vertical tilt in clouds on longer time scales. Hence, we conclude that tilt in
514 the moisture field is more robust than that in the omega field on the MJO time scale.

515 Previous work is also suggestive of more tilt in diabatic heating than we are finding,
516 during the TOGA COARE MJO. Especially, our results can be compared with Fig. 9 in
517 Lin et al. (2004, hereafter L04) and Fig. 12 in Kiladis et al. (2005, hereafter K05), in which
518 the TOGA COARE data set was analyzed in a similar lag-regression method to ours. These
519 studies examined diabatic heating (or Q1), which has a very similar structure to omega

520 (not shown). The major difference in results between these studies and ours is found in the
521 tailing edges of the event, where the L04 and K05 figures have more tilt. In Figs. 3 and 4,
522 we show our lag-regressed plot resembles the raw structure of the MJO with a simple time
523 filter. We believe that the relevant difference in methodology between their work and ours
524 is that both of the other studies used spatial filters in addition to time filters to obtain their
525 index time-series. Personal communication with Kiladis and Haertel confirmed that spatial
526 filtering was used in their analysis and that the difference of time versus time-space filters
527 makes non-negligible differences in the diabatic heating structures.

528 *d. Sensitivity of choice of filter*

529 Finally we will briefly discuss sensitivity of the choice of filters. Figure 8 illustrates the
530 response functions of the >1.5 day low-pass Lanczos filter and daily running mean filter.
531 This figure shows that by using the running mean filter, about 60% of the signals on 2 day
532 scale are lost due to the shallow slope of the response function. Even at 4 day period which
533 corresponds to the time scale of some of the Kelvin waves, about 20% of the signals are lost.
534 This indicates that for examining high frequency variability such as inertia gravity waves
535 or Kelvin waves, the Lanczos filter with a steeper slope of the response function is more
536 appropriate than the running mean filter.

537 **6. Conclusions**

538 We have examined the column-integrated moist static energy (MSE) budget during the
539 TOGA COARE field campaign, using sounding data, and filtering the data into various fre-
540 quencies of variability with ~ 2 day, ~ 5 day, ~ 10 day, and >20 day periodicity. In the deep
541 tropics, fluctuations of the column MSE are primarily due to variations of column-integrated
542 water vapor which are tightly connected with precipitation anomalies. Therefore, investi-
543 gating the mechanisms of recharge and discharge of the column MSE leads us to a better

544 understanding regarding the convective amplification and decay. Our analysis highlights the
545 importance of the investigation of the column MSE on different time scales. We found that
546 each budget term of the column MSE behaves in significantly different ways on the different
547 time scales. As a result, dominant processes in the MSE recharge and discharge differ among
548 the time scales. Some notable results are summarized as follows:

- 549 i. On all the time scales except for the MJO time scale, the vertical MSE advection,
550 $-\langle\omega\partial h/\partial p\rangle$, is the most dominant process with the greatest magnitude of variations
551 in the MSE recharge-discharge mechanism.
- 552 ii. On the shorter time scales (~ 2 day and ~ 5 day scales), the vertical MSE advection
553 accounts for most of the MSE recharge and discharge, and the other terms cancel out
554 each other so that the tendency of the column MSE $\langle\partial h/\partial t\rangle$ is primarily explained by
555 the vertical MSE advection.
- 556 iii. As the time scale gets longer, the relative importance of the other terms than the
557 vertical advection becomes greater. Especially on the MJO time scale, all the bud-
558 get terms (horizontal advection, $-\langle\vec{v}\cdot\nabla h\rangle$, vertical advection, $-\langle\omega\partial h/\partial p\rangle$, radiative
559 heating $\langle Q_R\rangle$, and surface fluxes SF) have nearly the same magnitude of variations.
- 560 iv. The horizontal advection behaves in significantly different ways among the different
561 time scales.
- 562 v. The amplitude of the horizontal advection becomes greater as the time scale get
563 longer, indicating that the horizontal advection plays a more important roll in the
564 MSE recharge-discharge mechanism on longer time scales than shorter time scales.
- 565 vi. The radiative heating is approximately in phase with the precipitation (or the pre-
566 cipitation leads slightly) while the surface fluxes lag the precipitation except for ~ 10
567 day scale on which both the radiative heating and surface fluxes are approximately in
568 phase with the precipitation.

569 vii. On the shorter time scales, the MSE export via vertical advection (i.e., positive
570 $\langle \omega \partial h / \partial p \rangle$) lags the precipitation peak. As the time scale gets longer, however, the
571 MSE export becomes more in phase with the precipitation.

572 The last bullet of the summary above, more in-phase MSE export via vertical advection,
573 is primarily explained by variations in the omega profile. The tilt of the profile at the
574 leading edge of the convection gets steeper as the time scale gets longer. This implies that
575 the second baroclinic structure of the omega profile becomes less robust in the early stage
576 of the convection. On the MJO time scale, the leading edge tilt becomes very steep, and
577 the overall omega structure becomes closer to the first baroclinic mode. Consequently, the
578 vertical component of the normalized gross moist stability (NGMS) becomes more a constant
579 quantity which is nearly independent of the convective life-cycle. In contrast, on the shorter
580 time scales where a second baroclinic mode is prominent, the vertical NGMS has large time-
581 dependency, thus the values of the vertical NGMS vary significantly along the convective
582 life-cycle. The horizontal component of the NGMS doesn't have a consistent pattern among
583 the different time scales since the horizontal MSE advection behaves in significantly different
584 ways on the different time scales.

585 Furthermore, our results shown in Fig. 2d, the MSE budgets in the MJO event, reinforce
586 the view of the MJO dynamics which has been emerging from recent MJO studies (e.g., Kim
587 et al. 2014; Sobel et al. 2014) in the following ways: 1) The radiative heating and surface
588 fluxes destabilize the MJO disturbance by amplifying and maintaining MSE anomalies. 2)
589 The vertical advection stabilizes the disturbance by exporting the MSE and canceling the
590 effects of the radiative heating and surface fluxes. 3) The horizontal advection plays a
591 significant role in the eastward propagation by providing moistening ahead (in the negative
592 lags, or to the east of), drying behind (in the positive lags, or to the west of) the active phase.
593 Although there are differences between the different MJO events, our results in general show
594 significant commonalities with those view points.

595 Finally, we should acknowledge again that we are uncertain about whether or not the
596 results shown for the longer time scale variability (~ 10 day and the MJO time scales)
597 represent statistically significant patterns because of the lack of the degrees of freedom.
598 Our results for the MJO timescale are broadly consistent with published work on MSE
599 budgets observed during the DYNAMO field campaign by Sobel et al. (2014), though we
600 find the vertical NGMS less variable over an MJO life-cycle, possibly due to our use of the
601 Lanczos filter rather than a running mean. For more accurate and solid conclusions, we need
602 to investigate more data sets such as ERA-Interim and TRMM which contain much longer
603 time-series than the TOGA COARE data. We would also like to repeat our analysis using
604 DYNAMO data in future work.

605 *Acknowledgments.*

606 We would like to thank Professor Gregory J. Tripoli and Professor Matthew H. Hitchman
607 for reading Kuniaki Inoue's M.S. thesis describing this study. We also thank Professor Adam
608 Sobel and Professor Hirohiko Masunaga for providing useful comments in a personal conver-
609 sation. Useful and constructive comments from two anonymous reviewers which improved
610 the original draft are gratefully acknowledged. Finally, we thank Dr. George N. Kiladis and
611 Dr. Patrick T. Haertel, who kindly reproduced their Q1 structure plots and clarified our
612 concern. This research is supported by NASA Grant NNX12AL96G.

REFERENCES

- 615 Andersen, J. A. and Z. Kuang, 2011: Moist static energy budget of MJO-like disturbances
616 in the atmosphere of a zonally symmetric aquaplanet. *J. Climate*, **25**, 2782–2804, doi:
617 10.1175/JCLI-D-11-00168.1.
- 618 Benedict, J. J., E. D. Maloney, A. H. Sobel, D. M. Frierson, and L. J. Donner, 2013: Tropical
619 intraseasonal variability in version 3 of the GFDL atmosphere model. *J. Climate*, **26**, 426–
620 449, doi:10.1175/JCLI-D-12-00103.1.
- 621 Benedict, J. J., E. D. Maloney, A. H. Sobel, and D. M. W. Frierson, 2014: Gross moist
622 stability and MJO simulation skill in three full-physics GCMs. *J. Atmos. Sci.*, doi:10.
623 1175/JAS-D-13-0240.1, in press.
- 624 Benedict, J. J. and D. A. Randall, 2007: Observed characteristics of the MJO relative to
625 maximum rainfall. *J. Atmos. Sci.*, **64**, 2332–2354, doi:10.1175/JAS3968.1.
- 626 Bretherton, C. S., M. E. Peters, and L. E. Back, 2004: Relationships between water vapor
627 path and precipitation over the tropical oceans. *J. Climate*, **17**, 1517–1528, doi:10.1175/
628 1520-0442(2004)017<1517:RBWVPA>2.0.CO;2.
- 629 Bretherton, C. S. and P. K. Smolarkiewicz, 1989: Gravity waves, compensating sub-
630 sidence and detrainment around cumulus clouds. *J. Atmos. Sci.*, **46**, 740–759, doi:
631 10.1175/1520-0469(1989)046<0740:GWCSAD>2.0.CO;2.
- 632 Bretherton, C. S., M. Widmann, V. P. Dymnikov, J. M. Wallace, and I. Blad, 1999: The
633 effective number of spatial degrees of freedom of a time-varying field. *J. Climate*, **12**,
634 1990–2009, doi:10.1175/1520-0442(1999)012<1990:TENOSD>2.0.CO;2.

- 635 Charney, J. G., 1963: A note on large-scale motions in the tropics. *J. Atmos. Sci.*, **20**,
636 607–609, doi:10.1175/1520-0469(1963)020<0607:ANOLSM>2.0.CO;2.
- 637 Charney, J. G., 1969: A further note on large-scale motions in the tropics. *J. Atmos. Sci.*,
638 **26**, 182–185, doi:10.1175/1520-0469(1969)026<0182:AFNOLS>2.0.CO;2.
- 639 Cho, H. and D. Pendlebury, 1997: Wave CISK of equatorial waves and the vertical distri-
640 bution of cumulus heating. *J. Atmos. Sci.*, **54**, 2429–2440, doi:10.1175/1520-0469(1997)
641 054<2429:WCOEWA>2.0.CO;2.
- 642 Duchon, C. E., 1979: Lanczos filtering in one and two dimensions. *J. Appl. Meteor.*, **18**,
643 1016–1022, doi:10.1175/1520-0450(1979)018<1016:LFIOAT>2.0.CO;2.
- 644 Frierson, D. M. W., 2007: Convectively coupled Kelvin waves in an idealized moist general
645 circulation model. *J. Atmos. Sci.*, **64**, 2076–2090, doi:10.1175/JAS3945.1.
- 646 Fu, X. and B. Wang, 2009: Critical roles of the stratiform rainfall in sustaining the
647 Madden-Julian Oscillation: GCM experiments*. *J. Climate*, **22**, 3939–3959, doi:10.1175/
648 2009JCLI2610.1.
- 649 Fuchs, Z. and D. J. Raymond, 2007: A simple, vertically resolved model of tropical dis-
650 turbances with a humidity closure. *Tellus A*, **59**, 344–354, doi:10.1111/j.1600-0870.2007.
651 00230.x.
- 652 Haertel, P. T. and G. N. Kiladis, 2004: Dynamics of 2-day equatorial waves. *J. Atmos. Sci.*,
653 **61**, 2707–2721, doi:10.1175/JAS3352.1.
- 654 Haertel, P. T., G. N. Kiladis, A. Denno, and T. M. Rickenbach, 2008: Vertical-mode decom-
655 positions of 2-day waves and the maddenjulian oscillation. *J. Atmos. Sci.*, **65**, 813–833,
656 doi:10.1175/2007JAS2314.1.

- 657 Hannah, W. M. and E. D. Maloney, 2011: The role of moisture-convection feedbacks in simu-
658 lating the maddenjulian oscillation. *J. Climate*, **24**, 2754–2770, doi:10.1175/2011JCLI3803.
659 1.
- 660 Hannah, W. M. and E. D. Maloney, 2014: The moist static energy budget in NCAR
661 CAM5 hindcasts during DYNAMO. *J. Adv. Model. Earth Syst.*, **6**, 420–440, doi:10.1002/
662 2013MS000272.
- 663 Kikuchi, K. and Y. N. Takayabu, 2004: The development of organized convection associated
664 with the MJO during TOGA COARE IOP: Trimodal characteristics. *Geophys. Res. Lett.*,
665 **31**, L10 101, doi:10.1029/2004GL019601.
- 666 Kiladis, G. N., K. H. Straub, and P. T. Haertel, 2005: Zonal and vertical structure of the
667 maddenjulian oscillation. *J. Atmos. Sci.*, **62**, 2790–2809, doi:10.1175/JAS3520.1.
- 668 Kiladis, G. N. and K. M. Weickmann, 1992: Circulation anomalies associated with trop-
669 ical convection during northern winter. *Mon. Wea. Rev.*, **120**, 1900–1923, doi:10.1175/
670 1520-0493(1992)120<1900:CAAWTC>2.0.CO;2.
- 671 Kiladis, G. N., M. C. Wheeler, P. T. Haertel, K. H. Straub, and P. E. Roundy, 2009: Convec-
672 tively coupled equatorial waves. *Rev. Geophys.*, **47**, RG2003, doi:10.1029/2008RG000266.
- 673 Kim, D., J.-S. Kug, and A. H. Sobel, 2014: Propagating versus nonpropagating Madden-
674 Julian oscillation events. *J. Climate*, **27**, 111–125, doi:10.1175/JCLI-D-13-00084.1.
- 675 Kim, D., et al., 2009: Application of MJO simulation diagnostics to climate models. *J.*
676 *Climate*, **22**, 6413–6436, doi:10.1175/2009JCLI3063.1.
- 677 Kuang, Z., 2008: A moisture-stratiform instability for convectively coupled waves. *J. Atmos.*
678 *Sci.*, **65**, 834–854, doi:10.1175/2007JAS2444.1.
- 679 Kuang, Z., 2010: The wavelength dependence of the gross moist stability and the scale

680 selection in the instability of column-integrated moist static energy. *J. Atmos. Sci.*, **68**,
681 61–74, doi:10.1175/2010JAS3591.1.

682 Lappen, C.-L. and C. Schumacher, 2012: Heating in the tropical atmosphere: what level
683 of detail is critical for accurate MJO simulations in GCMs? *Clim Dyn*, **39**, 2547–2568,
684 doi:10.1007/s00382-012-1327-y.

685 Lappen, C.-L. and C. Schumacher, 2014: The role of tilted heating in the evolution of the
686 MJO. *J. Geophys. Res. Atmos.*, **119**, 2966–2989, doi:10.1002/2013JD020638.

687 Lin, J., B. Mapes, M. Zhang, and M. Newman, 2004: Stratiform precipitation, vertical
688 heating profiles, and the maddenjulian oscillation. *J. Atmos. Sci.*, **61**, 296–309, doi:10.
689 1175/1520-0469(2004)061<0296:SPVHPA>2.0.CO;2.

690 Lin, J.-L., et al., 2006: Tropical intraseasonal variability in 14 IPCC AR4 climate models.
691 part i: Convective signals. *J. Climate*, **19** (12), 2665–2690, doi:10.1175/JCLI3735.1.

692 Lin, X. and R. H. Johnson, 1996: Kinematic and thermodynamic characteristics of the flow
693 over the western pacific warm pool during TOGA COARE. *J. Atmos. Sci.*, **53**, 695–715,
694 doi:10.1175/1520-0469(1996)053<0695:KATCOT>2.0.CO;2.

695 Maloney, E. D., 2009: The moist static energy budget of a composite tropical intraseasonal
696 oscillation in a climate model. *J. Climate*, **22**, 711–729, doi:10.1175/2008JCLI2542.1.

697 Mapes, B., S. Tulich, J. Lin, and P. Zuidema, 2006: The mesoscale convection life cycle:
698 Building block or prototype for large-scale tropical waves? *Dynamics of Atmospheres and*
699 *Oceans*, **42**, 3–29, doi:10.1016/j.dynatmoce.2006.03.003.

700 Mapes, B. E., 2000: Convective inhibition, subgrid-scale triggering energy, and stratiform
701 instability in a toy tropical wave model. *J. Atmos. Sci.*, **57**, 1515–1535, doi:10.1175/
702 1520-0469(2000)057<1515:CISSTE>2.0.CO;2.

703 Masunaga, H., 2012: Short-term versus climatological relationship between precipitation and
704 tropospheric humidity. *J. Climate*, **25**, 7983–7990, doi:10.1175/JCLI-D-12-00037.1.

705 Masunaga, H. and T. S. L’Ecuyer, 2014: A mechanism of tropical convection inferred from
706 observed variability in the moist static energy budget. *J. Atmos. Sci.*, **71**, 3747–3766,
707 doi:10.1175/JAS-D-14-0015.1.

708 Neelin, J. D. and I. M. Held, 1987: Modeling tropical convergence based on the moist
709 static energy budget. *Mon. Wea. Rev.*, **115**, 3–12, doi:10.1175/1520-0493(1987)115<0003:
710 MTCBOT>2.0.CO;2.

711 Neelin, J. D., O. Peters, and K. Hales, 2009: The transition to strong convection. *J. Atmos.*
712 *Sci.*, **66**, 2367–2384, doi:10.1175/2009JAS2962.1.

713 Peters, M. E. and C. S. Bretherton, 2006: Structure of tropical variability from a
714 vertical mode perspective. *Theor. Comput. Fluid Dyn.*, **20**, 501–524, doi:10.1007/
715 s00162-006-0034-x.

716 Raymond, D. J., 2000: Thermodynamic control of tropical rainfall. *Q.J.R. Meteorol. Soc.*,
717 **126**, 889–898, doi:10.1002/qj.49712656406.

718 Raymond, D. J. and Z. Fuchs, 2009: Moisture modes and the Madden-Julian oscillation. *J.*
719 *Climate*, **22**, 3031–3046, doi:10.1175/2008JCLI2739.1.

720 Raymond, D. J., S. L. Sessions, A. H. Sobel, and Z. Fuchs, 2009: The mechanics of gross
721 moist stability. *J. Adv. Model. Earth Syst.*, **1**, 9, doi:10.3894/JAMES.2009.1.9.

722 Sobel, A. and E. Maloney, 2012: An idealized semi-empirical framework for modeling the
723 Madden-Julian oscillation. *J. Atmos. Sci.*, **69**, 1691–1705, doi:10.1175/JAS-D-11-0118.1.

724 Sobel, A. and E. Maloney, 2013: Moisture modes and the eastward propagation of the MJO.
725 *J. Atmos. Sci.*, **70**, 187–192, doi:10.1175/JAS-D-12-0189.1.

- 726 Sobel, A., S. Wang, and D. Kim, 2014: Moist static energy budget of the MJO during
727 DYNAMO. *J. Atmos. Sci.*, **71**, 4276–4291, doi:10.1175/JAS-D-14-0052.1.
- 728 Sobel, A. H. and C. S. Bretherton, 2000: Modeling tropical precipitation in a single column.
729 *J. Climate*, **13**, 4378–4392, doi:10.1175/1520-0442(2000)013<4378:MTPIAS>2.0.CO;2.
- 730 Straub, K. H. and G. N. Kiladis, 2003: The observed structure of convectively coupled Kelvin
731 waves: Comparison with simple models of coupled wave instability. *J. Atmos. Sci.*, **60**,
732 1655–1668, doi:10.1175/1520-0469(2003)060<1655:TOSOCC>2.0.CO;2.
- 733 Sugiyama, M., 2009: The moisture mode in the quasi-equilibrium tropical circulation model.
734 part I: Analysis based on the weak temperature gradient approximation. *J. Atmos. Sci.*,
735 **66**, 1507–1523, doi:10.1175/2008JAS2690.1.
- 736 Takayabu, Y. N., K. Lau, and C. Sui, 1996: Observation of a quasi-2-day wave during
737 TOGA COARE. *Mon. Wea. Rev.*, **124**, 1892–1913, doi:10.1175/1520-0493(1996)124<1892:
738 OOAQDW>2.0.CO;2.
- 739 Velden, C. S. and J. A. Young, 1994: Satellite observations during TOGA COARE: Large-
740 scale descriptive overview. *Mon. Wea. Rev.*, **122**, 2426–2441, doi:10.1175/1520-0493(1994)
741 122<2426:SODTCL>2.0.CO;2.
- 742 Webster, P. J. and R. Lukas, 1992: TOGA COARE: The coupled ocean-atmosphere response
743 experiment. *Bull. Amer. Meteor. Soc.*, **73** (9), 1377–1416, doi:10.1175/1520-0477(1992)
744 073<1377:TCTCOR>2.0.CO;2.
- 745 Wu, Z., 2003: A shallow CISK, deep equilibrium mechanism for the interaction between
746 large-scale convection and large-scale circulations in the tropics. *J. Atmos. Sci.*, **60**, 377–
747 392, doi:10.1175/1520-0469(2003)060<0377:ASCDEM>2.0.CO;2.
- 748 Yanai, M., B. Chen, and W. Tung, 2000: The Madden-Julian oscillation observed dur-

749 ing the TOGA COARE IOP: Global view. *J. Atmos. Sci.*, **57**, 2374–2396, doi:10.1175/
750 1520-0469(2000)057<2374:TMJOOD>2.0.CO;2.

751 Yanai, M., S. Esbensen, and J.-H. Chu, 1973: Determination of bulk properties of tropical
752 cloud clusters from large-scale heat and moisture budgets. *J. Atmos. Sci.*, **30**, 611–627,
753 doi:10.1175/1520-0469(1973)030<0611:DOBPOT>2.0.CO;2.

754 Yu, J., C. Chou, and J. D. Neelin, 1998: Estimating the gross moist stability of the trop-
755 ical atmosphere*. *J. Atmos. Sci.*, **55**, 1354–1372, doi:10.1175/1520-0469(1998)055<1354:
756 ETGMSO>2.0.CO;2.

757 Zhang, M. H. and J. L. Lin, 1997: Constrained variational analysis of sounding data
758 based on column-integrated budgets of mass, heat, moisture, and momentum: Ap-
759 proach and application to ARM measurements. *J. Atmos. Sci.*, **54**, 1503–1524, doi:
760 10.1175/1520-0469(1997)054<1503:CVAOSD>2.0.CO;2.

761 **List of Tables**

762 1 Values of $\bar{\Gamma}$, $\bar{\Gamma}_h$, and $\bar{\Gamma}_v$ on each time scale

33

TABLE 1. Values of $\bar{\Gamma}$, $\bar{\Gamma}_h$, and $\bar{\Gamma}_v$ on each time scale

	~ 2 day scale	~ 5 day scale	~ 10 day scale	MJO scale
$\bar{\Gamma}$	0.26	0.25	0.20	0.33
$\bar{\Gamma}_h$	0.08	-0.02	-0.10	0.10
$\bar{\Gamma}_v$	0.18	0.25	0.29	0.20

763 List of Figures

764 1 (a): Power spectra of raw and filtered precipitation. Raw, ~ 2 day, ~ 5 day,
765 ~ 10 day, and >20 day (MJO) time scales are illustrated in gray, blue, green,
766 and black lines, respectively. (b): Response functions of Lanczos filters with
767 different cut-off frequencies. The colors are arranged in the same way as (a).
768 Thick solid lines represent theoretical responses of the filters and thin dash
769 lines show computed responses from the precipitation spectra. (c): Time
770 series of raw and filtered anomalous precipitation. The black line shows two
771 MJO events during TOGA COARE. 36

772 2 (Top panels): Lag auto-correlations of filtered precipitation (solid lines) and
773 lag correlations between filtered precipitation and filtered column MSE (dash
774 lines) on the four different time scales. (Bottom panels): Regression slopes
775 of anomalies of $\partial\langle h \rangle / \partial t$ (green), $-\langle \vec{v} \cdot \nabla h \rangle$ (gray dash), $-\langle \omega \partial h / \partial p \rangle$ (black),
776 $\langle Q_R \rangle$ (red), and SF (blue), regressed against filtered precipitation and scaled
777 with one standard deviation of the filtered precipitation on the different time
778 scales. The precipitation was filtered with (a) 1.5 \sim 3 day band-pass, (b) 3 \sim 7
779 day band-pass, (c) 7 \sim 20 day band-pass, and (d) >20 day low-pass filters. The
780 error bars on the left bottom corners in (a) and (b) represent average values
781 (among the lag time windows) of significant errors for each MSE budget term
782 computed with 90% significant level. The numbers on the right bottom corners
783 show estimated independent sample sizes on the different time scales. 37

784	3	Vertical structures of anomalous omega and wind divergence fields regressed	
785		against the filtered precipitation and scaled with one standard deviation of the	
786		filtered precipitation on ~ 2 day (a and b), ~ 5 day (c and d), ~ 10 day (e and	
787		f) and >20 day (g and h) scales. The contour interval of the omega plots is	
788		0.6×10^{-2} Pa/s, and that of the wind divergence plots is 0.5×10^{-6} s $^{-1}$. The areas	
789		surrounded by the green lines in the top two row panels correspond to the	
790		grids which passed correlation significance tests with 99% (on ~ 2 day scale)	
791		and 80% (on ~ 5 day scale) significant levels. The black dash lines illustrate	
792		tilting structures of the omega profiles on each time scale.	38
793	4	Anomalous omega profiles of the first MJO event during TOGA COARE with	
794		a 15-day running mean filter. The contour interval is 0.01 Pa/s.	39
795	5	Scaled lag regression slopes of vertical MSE advection (red), horizontal MSE	
796		advection (blue), and combination of those (green) during convective life-	
797		cycles as functions of scaled lag regression slopes of vertical DSE advection	
798		on different time scales. Each convective life-cycle starts from a filled circle,	
799		going around counterclockwise and terminates at a filled square. The dash	
800		lines illustrate Γ , Γ_h , and Γ_v at the precipitation peaks on different time scales	
801		which can be computed as the slopes of those lines.	40
802	6	Schematic figures of typical DSE and MSE profiles and shapes of the two	
803		dominant modes, Ω_1 and Ω_2 . Arrows illustrate air flows of convection and	
804		associated large-scale circulations. Leftward (rightward) arrows correspond	
805		to convergence (divergence).	41
806	7	As in Fig. 3, but for anomalous specific humidity. The contour intervals are	
807		0.6×10^2 J/kg for ~ 2 day (a) and ~ 5 day (b) scales, and 1.2×10^2 J/kg for ~ 10	
808		day (c) and the MJO (d) scales.	42
809	8	Response functions of >1.5 day low-pass Lanczos filter (with 151 points of	
810		weightings) and daily running mean filter.	43

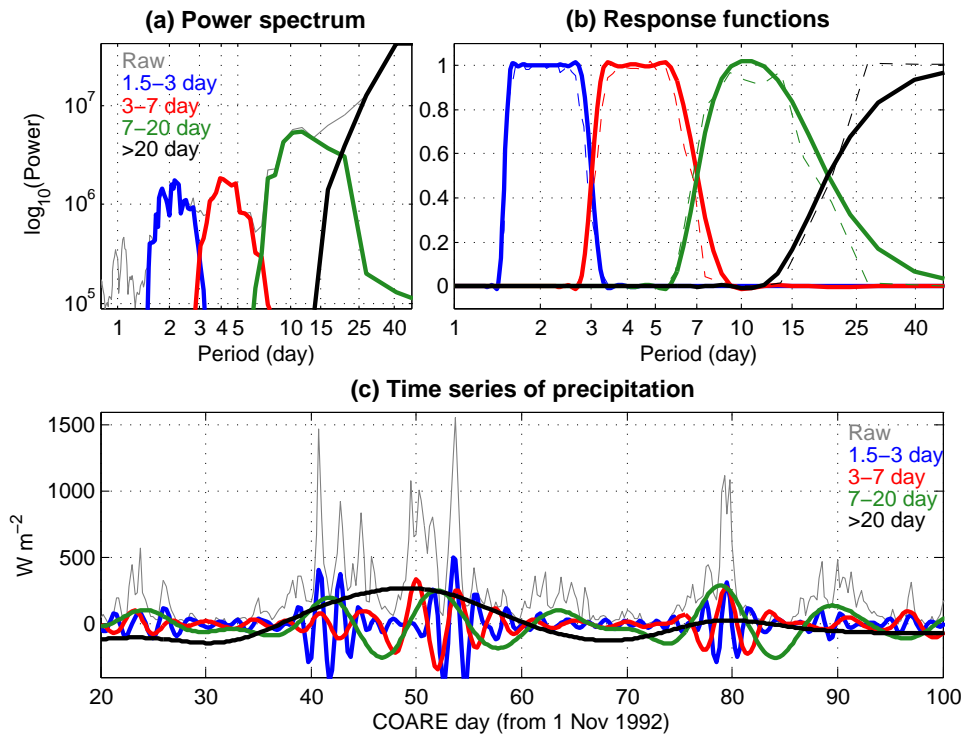


FIG. 1. (a): Power spectra of raw and filtered precipitation. Raw, ~ 2 day, ~ 5 day, ~ 10 day, and >20 day (MJO) time scales are illustrated in gray, blue, green, and black lines, respectively. (b): Response functions of Lanczos filters with different cut-off frequencies. The colors are arranged in the same way as (a). Thick solid lines represent theoretical responses of the filters and thin dash lines show computed responses from the precipitation spectra. (c): Time series of raw and filtered anomalous precipitation. The black line shows two MJO events during TOGA COARE.

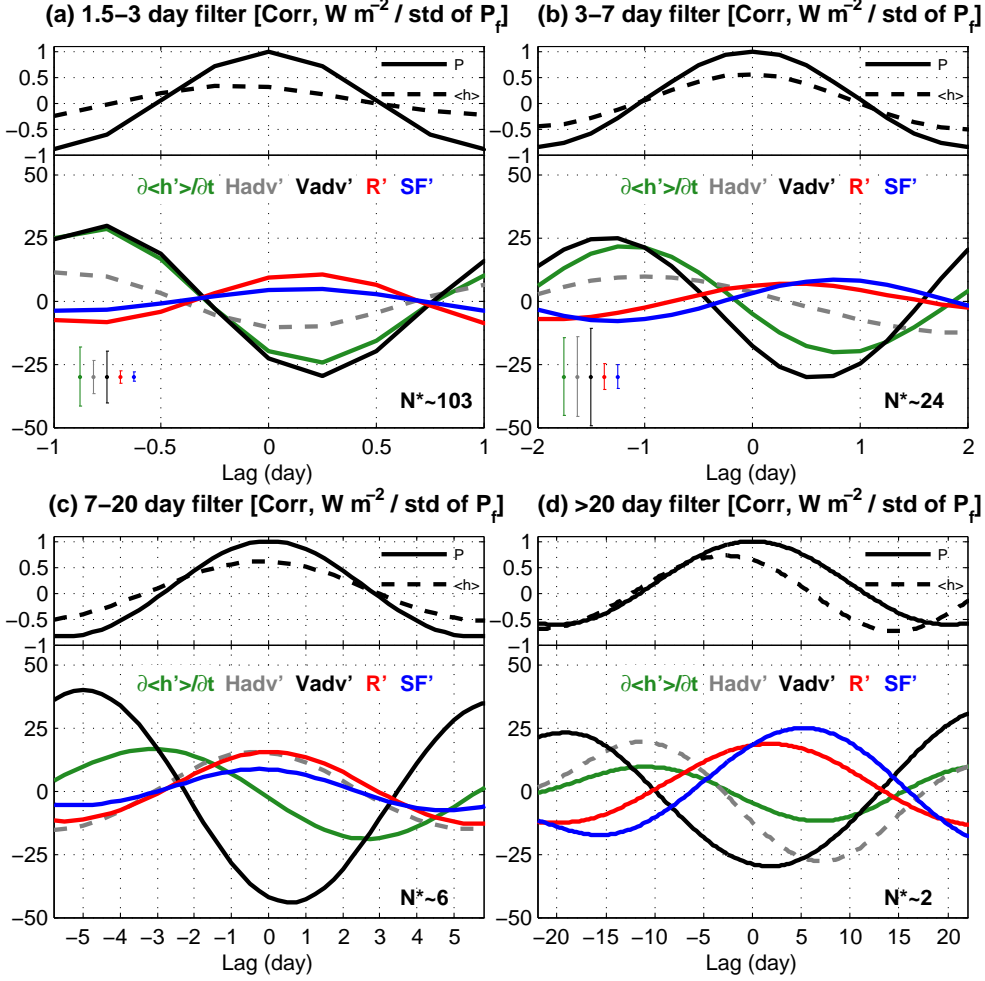


FIG. 2. (Top panels): Lag auto-correlations of filtered precipitation (solid lines) and lag correlations between filtered precipitation and filtered column MSE (dash lines) on the four different time scales. (Bottom panels): Regression slopes of anomalies of $\partial \langle h \rangle / \partial t$ (green), $-\langle \vec{v} \cdot \nabla h \rangle$ (gray dash), $-\langle \omega \partial h / \partial p \rangle$ (black), $\langle Q_R \rangle$ (red), and SF (blue), regressed against filtered precipitation and scaled with one standard deviation of the filtered precipitation on the different time scales. The precipitation was filtered with (a) 1.5~3 day band-pass, (b) 3~7 day band-pass, (c) 7~20 day band-pass, and (d) >20 day low-pass filters. The error bars on the left bottom corners in (a) and (b) represent average values (among the lag time windows) of significant errors for each MSE budget term computed with 90% significant level. The numbers on the right bottom corners show estimated independent sample sizes on the different time scales.

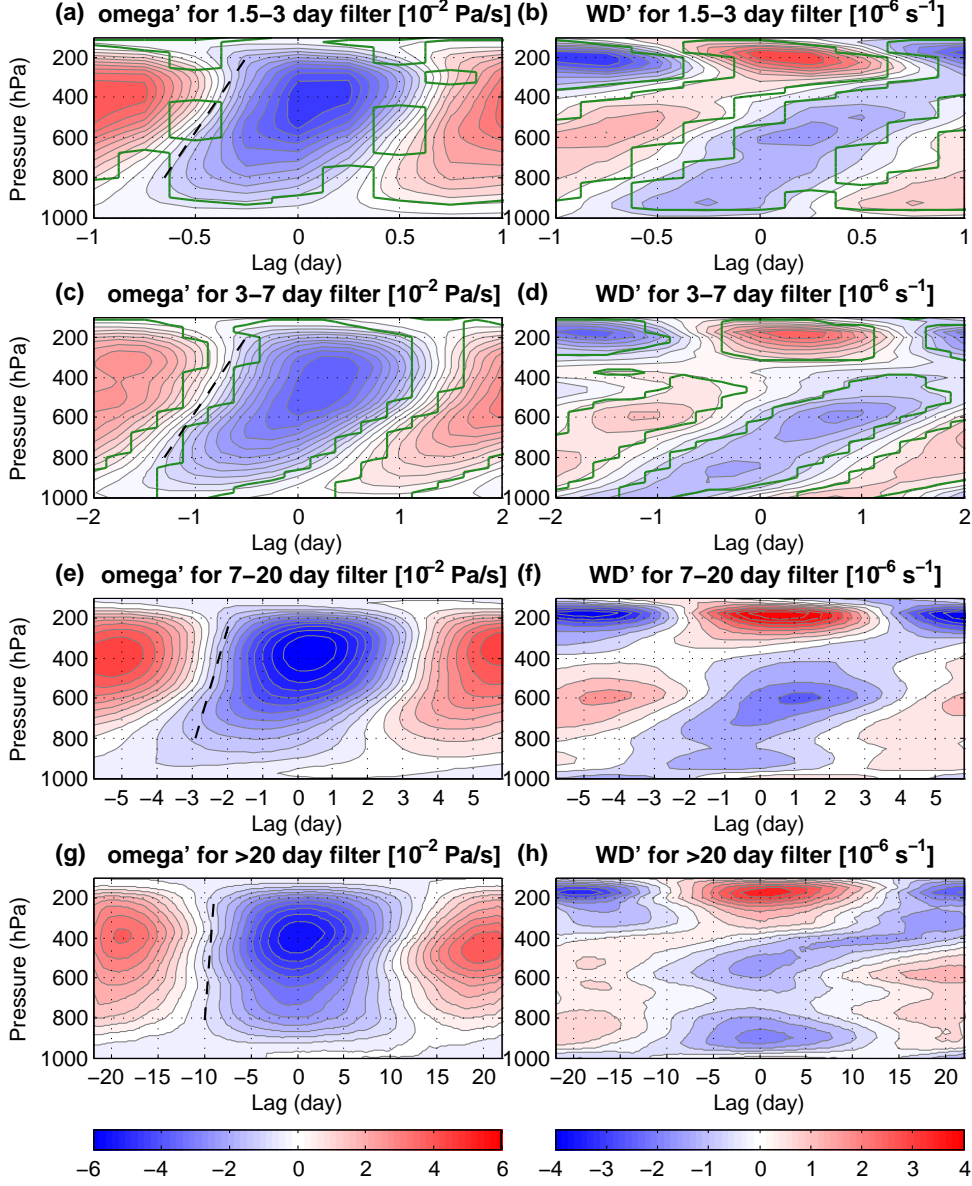


FIG. 3. Vertical structures of anomalous omega and wind divergence fields regressed against the filtered precipitation and scaled with one standard deviation of the filtered precipitation on ~ 2 day (a and b), ~ 5 day (c and d), ~ 10 day (e and f) and >20 day (g and h) scales. The contour interval of the omega plots is $0.6 \cdot 10^{-2}$ Pa/s, and that of the wind divergence plots is $0.5 \cdot 10^{-6}$ s^{-1} . The areas surrounded by the green lines in the top two row panels correspond to the grids which passed correlation significance tests with 99% (on ~ 2 day scale) and 80% (on ~ 5 day scale) significant levels. The black dash lines illustrate tilting structures of the omega profiles on each time scale.

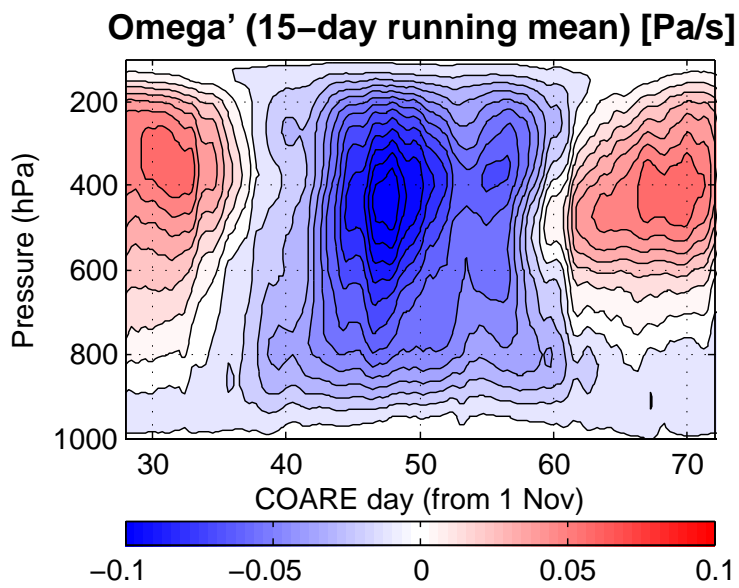


FIG. 4. Anomalous omega profiles of the first MJO event during TOGA COARE with a 15-day running mean filter. The contour interval is 0.01 Pa/s.

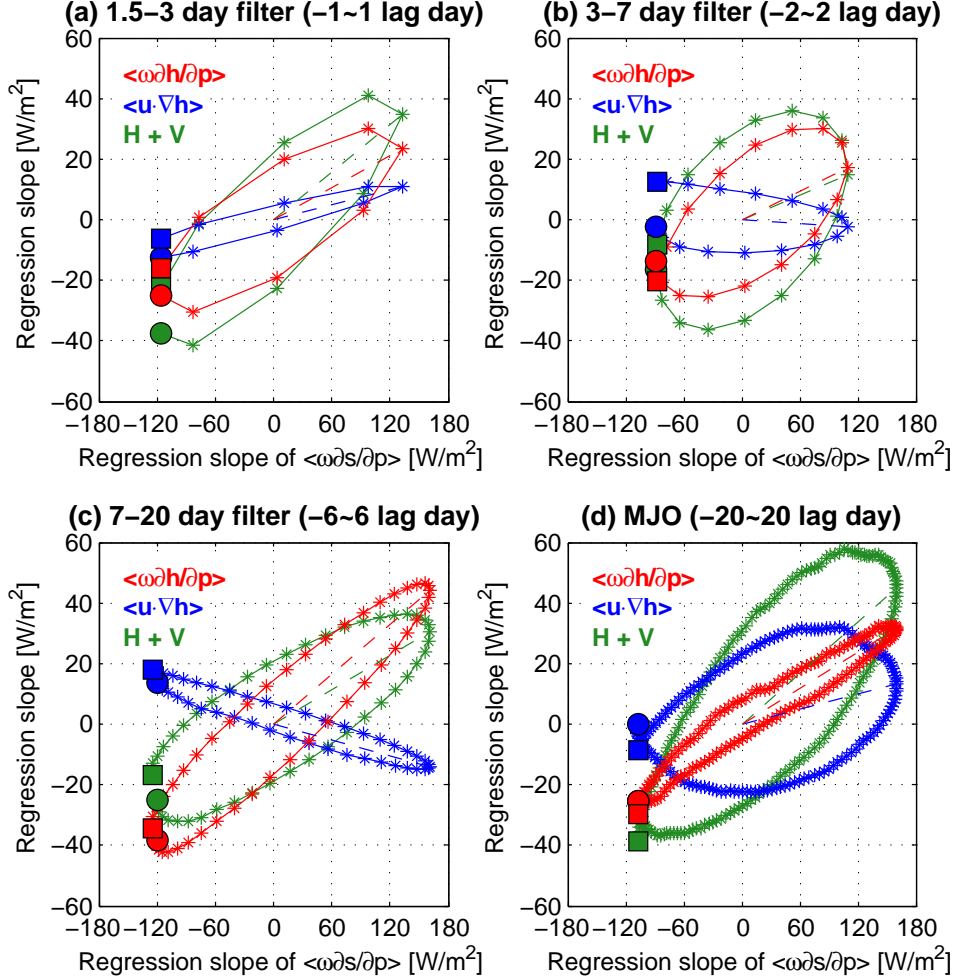


FIG. 5. Scaled lag regression slopes of vertical MSE advection (red), horizontal MSE advection (blue), and combination of those (green) during convective life-cycles as functions of scaled lag regression slopes of vertical DSE advection on different time scales. Each convective life-cycle starts from a filled circle, going around counterclockwise and terminates at a filled square. The dash lines illustrate Γ , Γ_h , and Γ_v at the precipitation peaks on different time scales which can be computed as the slopes of those lines.

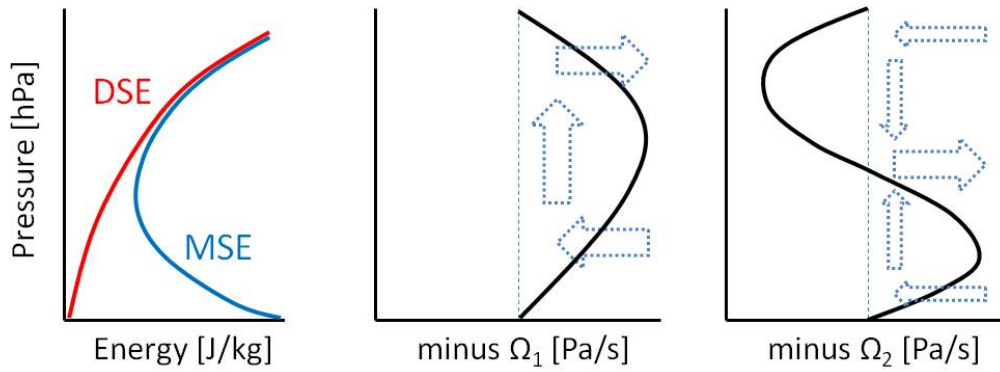


FIG. 6. Schematic figures of typical DSE and MSE profiles and shapes of the two dominant modes, Ω_1 and Ω_2 . Arrows illustrate air flows of convection and associated large-scale circulations. Leftward (rightward) arrows correspond to convergence (divergence).

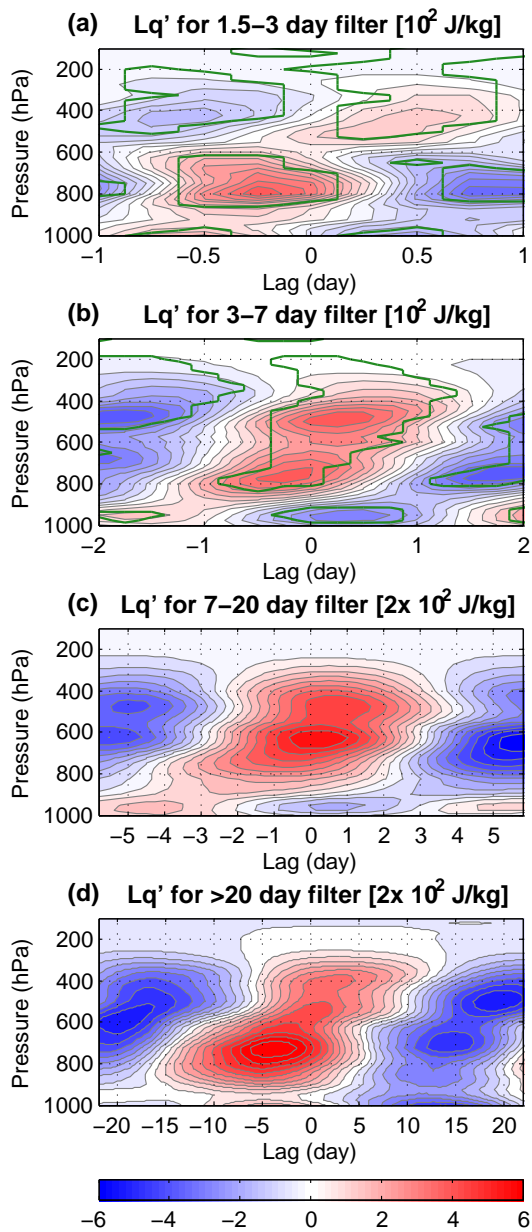


FIG. 7. As in Fig. 3, but for anomalous specific humidity. The contour intervals are $0.6 \cdot 10^2$ J/kg for ~ 2 day (a) and ~ 5 day (b) scales, and $1.2 \cdot 10^2$ J/kg for ~ 10 day (c) and the MJO (d) scales.

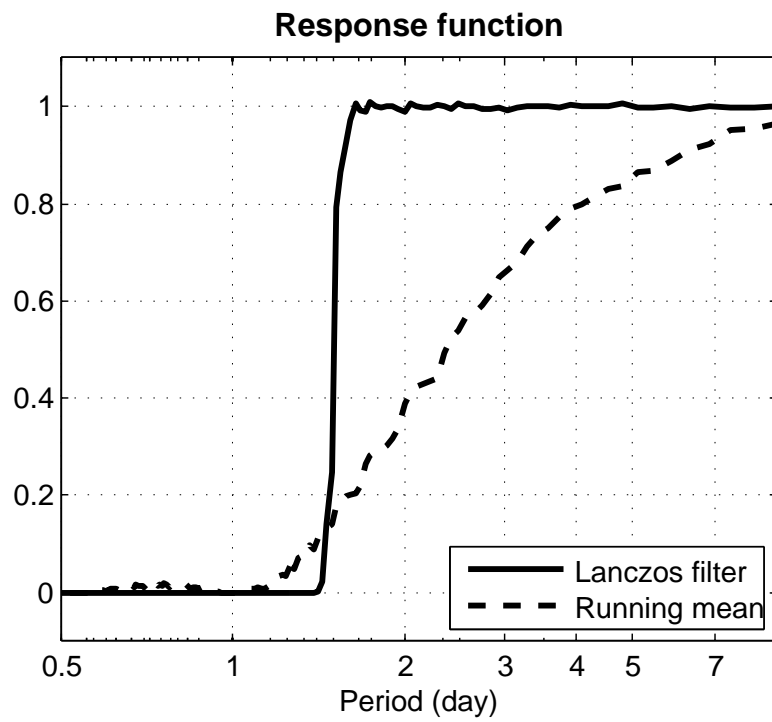


FIG. 8. Response functions of >1.5 day low-pass Lanczos filter (with 151 points of weightings) and daily running mean filter.